

Structural basis for DNA proofreading

Received: 3 August 2023

Accepted: 4 December 2023

Published online: 27 December 2023

 Check for updatesGina Buchel^{1,2}, Ashok R. Nayak^{1,2}, Karl Herbine¹, Azadeh Sarfallah¹, Viktoriia O. Sokolova¹, Angelica Zamudio-Ochoa¹ & Dmitry Temiakov¹✉

DNA polymerase (DNAP) can correct errors in DNA during replication by proofreading, a process critical for cell viability. However, the mechanism by which an erroneously incorporated base translocates from the polymerase to the exonuclease site and the corrected DNA terminus returns has remained elusive. Here, we present an ensemble of nine high-resolution structures representing human mitochondrial DNA polymerase Gamma, Pol γ , captured during consecutive proofreading steps. The structures reveal key events, including mismatched base recognition, its dissociation from the polymerase site, forward translocation of DNAP, alterations in DNA trajectory, repositioning and refolding of elements for primer separation, DNAP backtracking, and displacement of the mismatched base into the exonuclease site. Altogether, our findings suggest a conserved ‘bolt-action’ mechanism of proofreading based on iterative cycles of DNAP translocation without dissociation from the DNA, facilitating primer transfer between catalytic sites. Functional assays and mutagenesis corroborate this mechanism, connecting pathogenic mutations to crucial structural elements in proofreading steps.

Maintaining fidelity of replication of genetic information is among the most critical functions of living organisms. Errors arise as a result of DNA damage but also owing to the occasional incorporation of incorrect (non-cognate) substrates, resulting in mismatched base pairs and potentially deleterious mutations¹. Cells have evolved sophisticated mechanisms to fix these errors²; among them is the ability of DNAP to correct the mismatched bases during DNA replication by a proofreading activity^{3–5}. Proofreading employs an intrinsic exonucleolytic activity present in DNAP, or the exonucleolytic activity of auxiliary factors^{6,7}. The former is observed in the Pol A family of DNAPs, which includes bacterial DNA Polymerase I, bacteriophage T7 DNAP, and human mitochondrial DNAP Pol γ ^{4,8–12}. The N-terminus of these polymerases harbors an exonuclease domain capable of excision of a terminal nucleotide in a canonical metal ion-dependent reaction¹³. The exonuclease (*exo*) site is located ~ 35 Å away from the polymerase (*pol*) site, with no direct path between them. Therefore, it remains unclear how the misincorporated nucleotide in the nascent DNA can be transferred into the *exo* site, what triggers the primer separation from the template strand, and how the corrected terminus returns to the *pol* site after the cleavage^{6,14,15}. One of the hypotheses is based on an intermolecular model, which postulates that upon incorporating a

non-cognate base, DNAP dissociates and rebinds the mismatched primer in the *exo* site^{16,17}. Alternative models suggest an intramolecular mode of proofreading, during which polymerase stays associated with the DNA, but the primer terminus shifts from the *pol* site to the *exo* site and returns^{18–21} or a combination of the two modes¹⁴. While there is a general agreement in the field that Pol A enzymes are processive and can proofread DNA without dissociating, the lack of understanding of how editing can be achieved without the engagement of dedicated structural elements in DNAP has persisted until now^{6,14,15}. In this study, we provide a structural basis for the mechanism of proofreading, termed here as “bolt-action,” by human mitochondrial DNAP Pol γ and describe the major steps of this process.

Results and discussion

Capturing Pol γ during the multi-step proofreading process

To study the proofreading mechanism, we hypothesized that if a processive DNAP, such as Pol γ , does not dissociate from the DNA template, it must traverse the misincorporated base from the *pol* to the *exo* site through intermediate steps. Two strategies were used to capture these intermediates by preventing the exonucleolytic activity of the enzyme. In the first, we used Wild Type (WT) Pol γ (Fig. 1a) and a

¹Department of Biochemistry and Molecular Biology, Thomas Jefferson University, 1020 Locust St, Philadelphia, PA 19107, USA. ²These authors contributed equally: Gina Buchel, Ashok R. Nayak. ✉e-mail: dmitry.temiakov@jefferson.edu

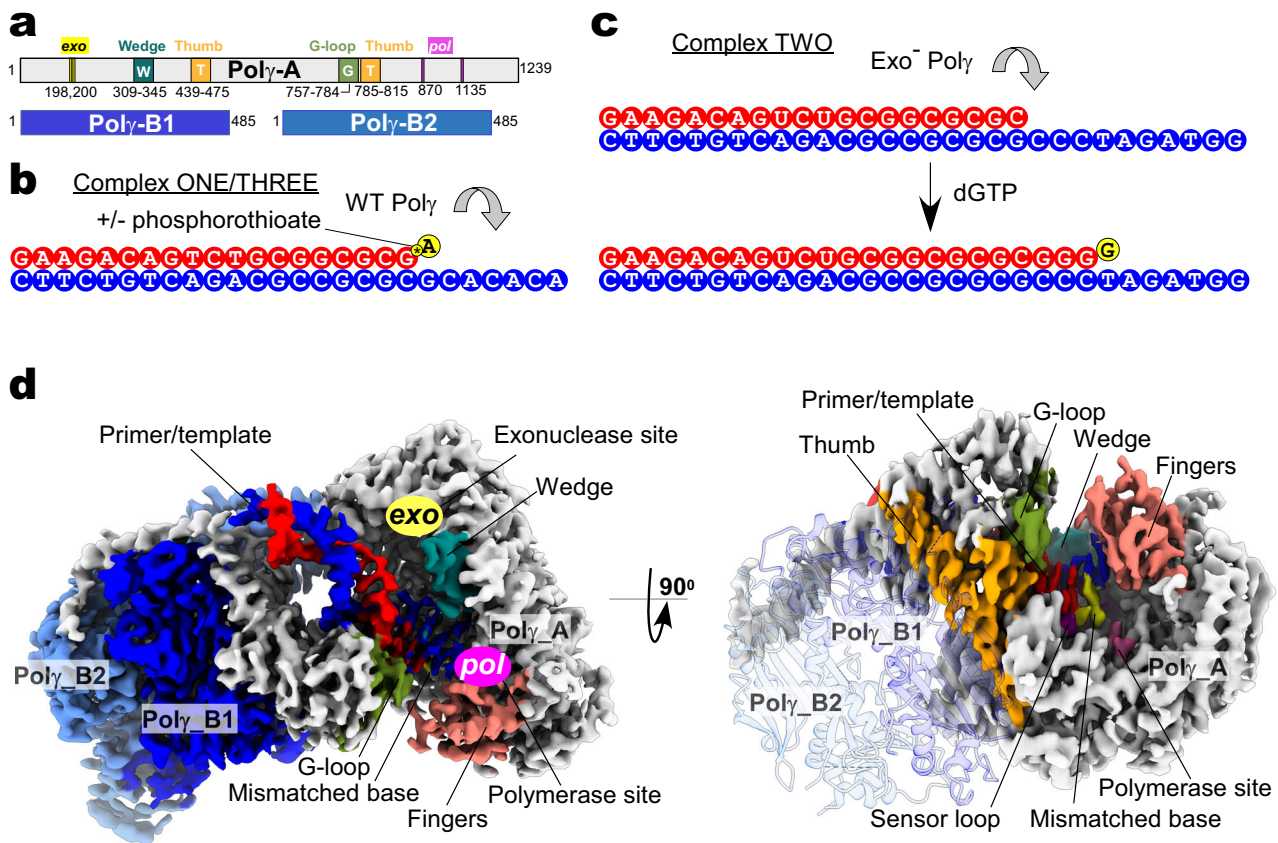


Fig. 1 | CryoEM structure of Poly. **a** A schematic showing the domain organization of the Poly holoenzyme. Poly_A subunit is in white, Poly_B1 in royal blue, and Poly_B2 in sky blue. **b, c** Assembly of the editing complexes. DNA template strand (here and throughout) is shown in blue, the primer is in red, and the mismatched base is in yellow. **d** CryoEM density map of Poly Mismatch Sensing complex

(Structure I) at 2.8 Å. The Poly_B homodimer is shown as a ribbon model (right panel) to reveal the Thumb subdomain (orange). The polymerase (*pol*) site is colored pink, and the exonuclease (*exo*) site is yellow. Major structural elements involved in proofreading - Wedge (teal), Guide loop (G-loop, smudge), and Sensor loop (purple)—are shown.

synthetic DNA scaffold with a primer having a terminal mismatched base connected via a nonhydrolyzable phosphorothioate bond (Complex ONE, Fig. 1b). In the second, we used a variant of Poly, in which the catalytic residues in the *exo* site have been mutated¹² (D198A/E200A, Exo⁻ Poly), and an RNA-DNA scaffold (Complex TWO, Fig. 1c). The primer in this complex has been extended by incorporating three cognate dGMP nucleotides and misincorporating one dGMP nucleotide against dTMP, generating a terminal mismatched base pair (Fig. 1c). Both complexes showed no significant exonuclease primer degradation within the time frame of the experiment (Supplementary Fig. 1a, b). In addition, to validate the data obtained using complex ONE, we prepared WT Poly complex, in which ~60% of the mismatched DNA primer, containing hydrolyzable phosphodiester bond, has undergone proofreading (Complex THREE, Supplementary Fig. 1c).

The complexes were subjected to single-particle analysis using cryogenic-electron microscopy (CryoEM) (Supplementary Fig. 2–6, Supplementary Tables 1, 2). A series of high-resolution structures ranging from 2.6 to 3.1 Å provides a detailed account of the proofreading process (Figs. 1d and 2a, Supplementary Figs. 7 and 8). The CryoEM data revealed that Complex ONE and THREE were represented by five major 3D classes, while Complex TWO—by four major 3D classes, each with a conformation different from the one found in the catalytic Poly complexes published previously^{8,22} (Supplementary Figs. 2–6). Complexes ONE and THREE data sets produced a structure with a mismatched base in the *pol* site (Structure I, “Mismatch Sensing” complex), a structure with the mismatched base uncoupled from the *pol* site (Structure II, “Mismatch Uncoupling” complex), a structure

with Poly during initial backward translocation toward the *exo* site (Structure VII, “Backtracking Initiation” complex), a structure with a mismatched base at the entrance of the exonucleolytic channel (Structure VIII, “Wedge Alignment” complex), and a structure with two single-stranded nucleotides of the primer located in the exonucleolytic channel (Structure IX, “Primer Separation” complex) (Fig. 2a, Supplementary Figs. 2, 4, and 7a). Analysis of the Complex TWO dataset resulted in structures representing the consequent forward translocation of Poly relative to the conformation observed in Structure II by one base pair (bp) (Structure III, “Mismatch Locking” complex) and by two bp (Structures IV, V and VI, “Guide Loop Engagement” complex) (Fig. 2a, Supplementary Figs. 3 and 7b). Structures IV–VI reveal the same location of the mismatched base of the primer relative to the catalytic sites but show notable changes in protein conformation (Supplementary Fig. 7b). Overall, the ensemble of structures represents a stepwise progression of the proofreading process with a single-nucleotide resolution (Fig. 2a, Supplementary Figs. 7 and 8, Supplementary Videos 1 and 2). At the beginning of the proofreading process, the mismatched base is located in the *pol* site (Structure I); upon completion of the primer’s translocation, this base is found ~35 Å away in the *exo* site (Structure IX) (Fig. 2b). The remaining structures represent the consecutive steps along the primer translocation pathway, which were assigned based on the proximity of the 3’ end of the primer to the *pol* or *exo* site (Fig. 2b). The non-overlapping conformational states of the Poly-DNA complexes reveal that upon recognition of the mismatched base and its removal from the *pol* site (Structures I and II), Poly translocates forward until the 3’ end of the primer is positioned at the entrance to the channel that leads to the *exo*

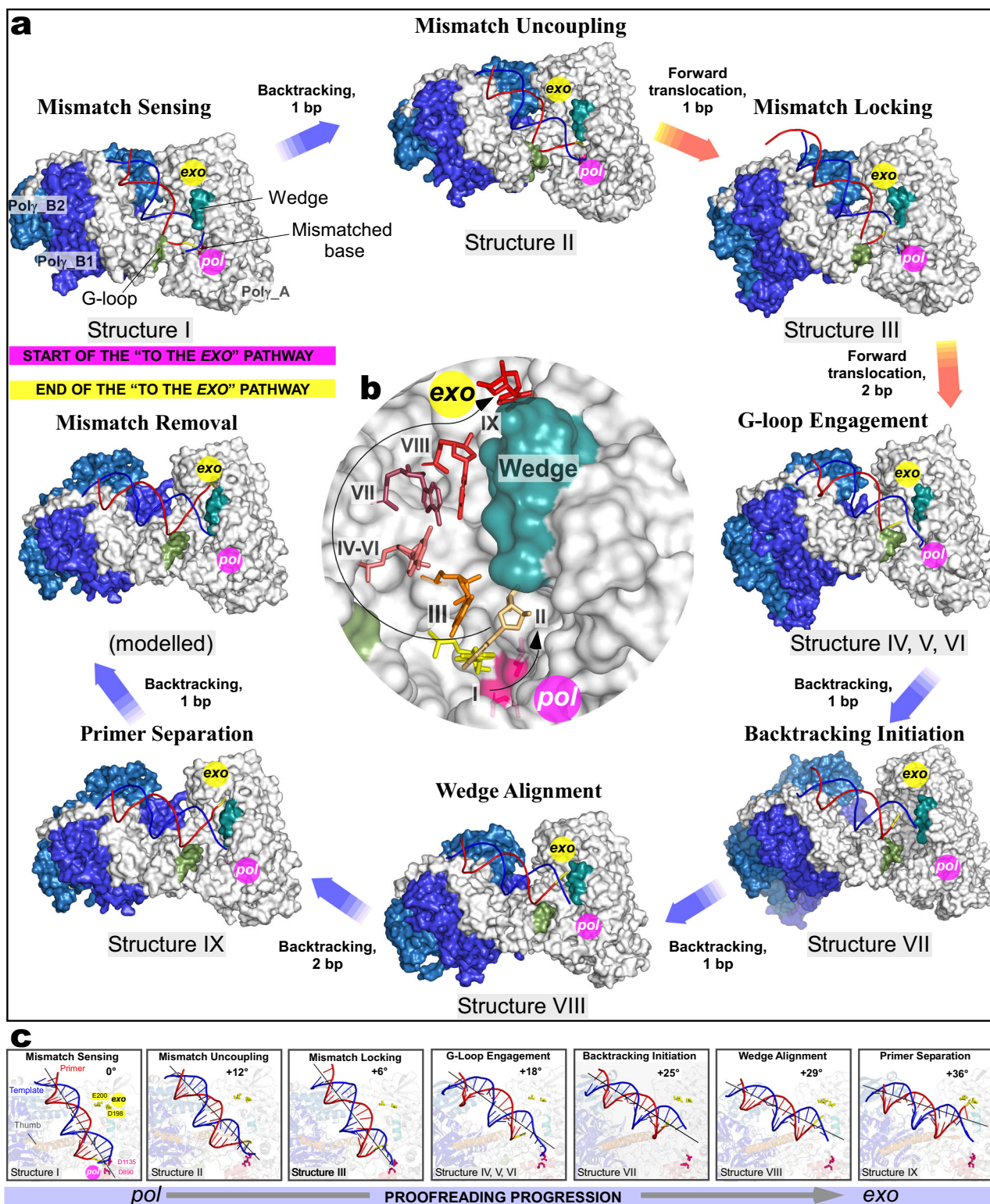


Fig. 2 | CryoEM captures multiple steps along the DNA proofreading pathway.

a Poly structures representing the major steps of the proofreading process. The complexes (Structures I–IV, VII, VIII, and IX, surface representation) are shown in the same orientation of their catalytic subunits. The Mismatch Removal complex is modeled using Structure IX to illustrate the final step of the proofreading. **b** The

trajectory of the mismatched base during proofreading. The structures were aligned using the Poly_A subunits. The mismatched base of the primer is shown. **c** The change of DNA trajectory during proofreading. Structures are shown in the same orientation of their catalytic subunit. Change in DNA trajectory (degrees) is indicated relative to the DNA axis in the Mismatch-Sensing complex.

site (Structures III, IV, V, and VI, Fig. 2a). The transition from the Mismatch Uncoupling to the Mismatch Locking complex requires forward translocation of Poly by one bp without major conformational changes (Supplementary Videos 3, 4). This suggests that Structures III–VI, obtained from analysis of the Complex TWO dataset, represent proofreading steps that follow the Mismatch Uncoupling but precede conformations captured in Structures VII–IX from Complex ONE (Fig. 2a, Supplementary Videos 1, 2). Upon positioning the 3' end of the primer at the entrance of the exonuclease channel, Poly translocates backward (Structure VII) to juxtapose the Wedge helix in the exonuclease domain next to the mismatched base pair (Structure VIII) and then to separate the 3' end of the primer from the template and divert it towards the *exo* site in Structure IX (Fig. 2).

The final step of proofreading (Fig. 2a, “Mismatch Removal”) and the corresponding structure have not been captured in our data sets due to experimental design since either the *exo* site (Complex TWO) or the 3' terminus of the primer (Complex ONE) has been modified, affecting the affinity of the 3' end of the primer towards the *exo* site. Nevertheless, the position of the primer termini poised for endonucleolytic reaction can be modeled based on the existing structure of the Klenow fragment of DNAP⁴. The progression of Poly along the proofreading pathway is accompanied by -40° change in the DNA axis relative to DNA in the catalytic structure (Fig. 2c) and by the relative motion of its subunits discussed below. Altogether, the observed conformations of Poly represent consecutive steps in the process of translocation of the 3' end of the primer from the *pol* site to the *exo* site (Fig. 2a, b), consistent with a non-dissociative (intramolecular) model of proofreading.

Mismatch sensing and uncoupling from the *pol* site

The Complex ONE dataset revealed the initial stages of mismatch recognition (Fig. 3a), most likely because the phosphorothioate in the primer slows down the kinetics of DNAP translocation¹³. Structure I (Mismatch-Sensing complex, Fig. 3a) represents the open post-translocated conformation of the primer-template complex, in which the fingers subdomain (res 942–983) is disengaged from DNA. The mismatched base is found in the *pol* site at about the same distance from the catalytic aspartate residues as the cognate base²² but tilted as compared to the canonical Watson-Crick base-pairing (Fig. 3c, d). The mismatched base pair is sensed via minor groove interactions with R853 and Q1102 residues, which are the functional analogs of R615 and Q797 in *Bacillus* DNAP I²³, and R429 and Q615 in T7 DNAP⁹. The interaction with the mismatch-sensing R853 residue is lost, but new hydrogen bonds are formed with the Q1102 residue of Poly_A, altering the geometry of the terminal base pair (Fig. 3c). In addition, the Y955 residue of the O helix, which is also implicated in correct base-pairing sensing²⁴, partially occupies the substrate insertion site, impairing the extension of the mismatched primer (Fig. 3c).

Following mismatch recognition, the mismatched base is relocated -15 \AA away from the catalytic aspartate residues in the *pol* site in Structure II (Mismatch Uncoupling complex, Fig. 3b). Alignment of Structure I and II using the Poly_B homodimer suggests that the upstream contacts of Poly with the DNA are preserved and reveal the backward translocation of DNAP (Fig. 3e). This translocation is accompanied by a rigid body 9° rotation of the palm subdomain of the Poly_A subunit relative to the thumb subdomain of Poly_A, which remains bound to the upstream DNA (Supplementary Video 3). Movement of the Poly_A palm subdomain around the axis nearly perpendicular to the DNA axis, accompanied by translocation of Poly along the DNA, positions the 3' end of the primer 15 \AA away from the catalytic aspartate residues in the *pol* site (Fig. 3e). Alignment of Structure I and II using the conserved palm subdomain (res 815–910 and 1095–1236) suggests the movement of the “Sensor loop” (res 851–870), which harbors the mismatch-recognition residue R853 (Fig. 3f, g). Residues 861–864 of the Sensor loop are bulging away from

their position in the *pol* site of the Mismatch-Sensing complex, making its position incompatible with the primer trajectory in Structure I and contributing to the uncoupling of the mismatched base from the *pol* site (Fig. 3f, g).

Forward translocation of Poly during proofreading

Alignment of the Poly_B homodimers in Structures II and III reveals the next step of proofreading (Mismatch Locking complex, Structure III), where forward translocation of Poly by one base pair along the DNA axis is observed (Fig. 3h, Supplementary Video 4). Poly moves as a rigid body, not affecting the relative trajectory of the DNA (RMSD 0.8 \AA for 1335 C α atoms). Six bases of the template strand of DNA are seen to neatly fit within the binding cavity of Poly_A between the fingers and thumb subdomains in the Mismatch Locking complex (Fig. 4a, b). The first unpaired template base ($n+1$) is flipped out and partially stacks the mismatched base, assuming a “locking” conformation (Fig. 4a, b). The stacking interaction of the locking base with the mismatched base of the primer may prevent the premature fraying of the latter and its separation from the DNA template, ensuring timely entry to the exonuclease channel. The conformation of primer/template in Poly observed in the Mismatch Locking complex is additionally stabilized by interactions with two conserved arginine residues (R337, R338) in the Wedge helix extension region, which becomes ordered in Structure III, and N803 and R807 residues in the thumb subdomain (Fig. 4a, b).

The subsequent step in the proofreading pathway involves forward translocation of Poly along the DNA axis, rotation of the Poly_A subunit relative Poly_B homodimer, and refolding of the structural element termed the “Guide loop” (or G-loop, res 757–784), resulting in another distinct Poly conformation (G-loop Engagement complex, Structure IV, Fig. 4c, d, Supplementary Video 5). As in Structure III, the DNA binding cavity of Poly_A in the G-loop Engagement complex accommodates 6 bp of the single-stranded template DNA, which now runs nearly parallel to the Wedge helix (Fig. 4c). The $n+1$ base completes its rotation and is in a nearly perfect stacking conformation with the mismatched base (Fig. 4d), which likely limits any further forward translocation of Poly. Compared to Structure III, the palm of Poly_A gradually rotates relative to its thumb subdomain and Poly_B2 by 13° – 26° (Fig. 4c), assuming its most “open” conformation and changing the trajectory of DNA by 15° within the catalytic subunit in Structure VI (Fig. 2c). The distance between Poly_B2 and the catalytic subunit increases to -17 \AA as measured by the position of the Arg 232 residue, which sits within the interacting distance with E394 residue in Poly_B2 in Structures I–III (Fig. 4e). In contrast, the later steps (Structures IV–IX) show a significantly enlarged gap between them in the “open” conformation of Poly (Fig. 4e). This relative movement of Poly subunits appears critical for proofreading activity as it opens up the path for the primer toward the *exo* site, as has been proposed earlier¹⁷.

The palm rotation of the Poly_A subunit is accompanied by alterations in the thumb subdomain, which changes from a bent to a straight conformation (Fig. 4f, Supplementary Video 5). Alignment of the palm subdomains of Poly_A in Structures IV and III shows the G-loop translation of -14 \AA and the fingers subdomain rotation by 15° , which pushes the 3' terminus of the primer toward the *exo* site (Fig. 4b, d, g). A conserved residue in the G-loop, K768, is observed making a hydrogen bond with the phosphate backbone of the primer, moving -13 \AA from its position in Structure III. To probe the functional importance of the G-loop for proofreading activity of Poly, we generated a deletion variant lacking residues 761–769 (Δ G-loop Poly). We found that the enzyme's binding affinity (Supplementary Fig. 9a–c) and catalytic activity (Supplementary Fig. 9d) were not affected by this deletion. Because the base of the G-loop contributes to Poly interactions with the DNA primer during primer extension, deletion of the G-loop residues results in a notable decrease in the rate of translocation (Fig. 4h). Importantly, Δ G-loop Poly showed dramatically impaired

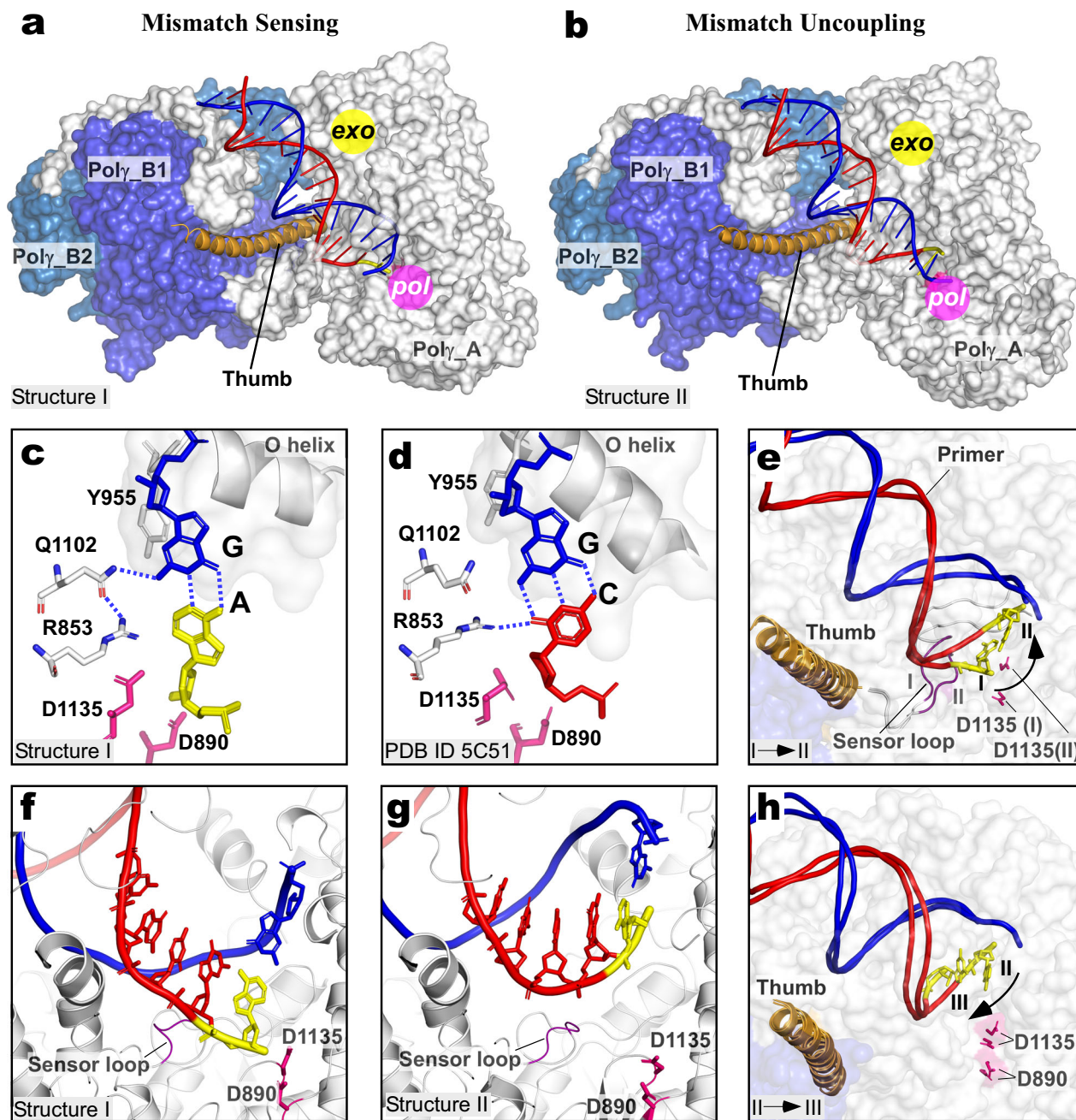


Fig. 3 | Mismatched base sensing and uncoupling from the *pol* site. **a, b** Structures of the Mismatch-Sensing and Uncoupling complexes. The Poly structures (surface representation) are shown in the same orientation of the Poly_B homodimer. The thumb domain (res 439–476, orange) is shown as a ribbon representation. Parts of the N-terminal domain of Poly_A (476–495, 592–623) and thumb (res 797–811) are omitted for clarity. **c, d** Close-up views of the *pol* active sites of the mismatched sensing (**c**) and catalytic (PDB ID 5C51, **d**) complexes. The complexes were shown in the same orientation of their conserved palm subdomains, the catalytic *pol* site residues (D890/D1135) are in pink. **e** A close-up view

of DNA in the Mismatch-Sensing and Mismatch Uncoupling complexes. The structures were aligned using their Poly_B homodimers. The mismatched bases are indicated in yellow, and the bulging part of the Sensor loop (res 861–864) is shown in purple. **f, g** Close-up views of the DNA binding cavity in Mismatched Sensing (**a**) and Mismatch Uncoupling (**b**) complexes. The complexes are shown in the same orientation of the conserved palm subdomain. **h** Poly transition from Mismatch Uncoupling to Mismatch Locking complex. The structures were aligned using their Poly_B homodimers. DNA strands and mismatched bases (yellow) are shown.

exonucleolytic activity on the mismatched scaffold, confirming the key role of the G-loop in proofreading (Fig. 4i). As mentioned above, Structures IV–VI show similar overall conformations (Fig. 4c). The most notable difference between these conformations is the gradual motion of the G-loop (Fig. 4g), accompanied by the straightening of the thumb and rotation of the palm subdomain of the Poly_A subunit, suggesting an essential role of these elements in the proofreading process.

Poly backtracking and primer separation

The transition to the G-loop Engagement complex aligns the 3' end of the mismatched primer with the entrance to the narrow channel leading to the *exo* site (Fig. 4c). Backward translocation of Poly is now needed to separate the primer from the template strand and to deliver the mismatched base into the *exo* site (Fig. 5a–c). In the Backtracking Initiation complex, Poly has translocated 1 bp backward as compared to the G-loop Engagement complex observed in Structure VI (Fig. 5a,

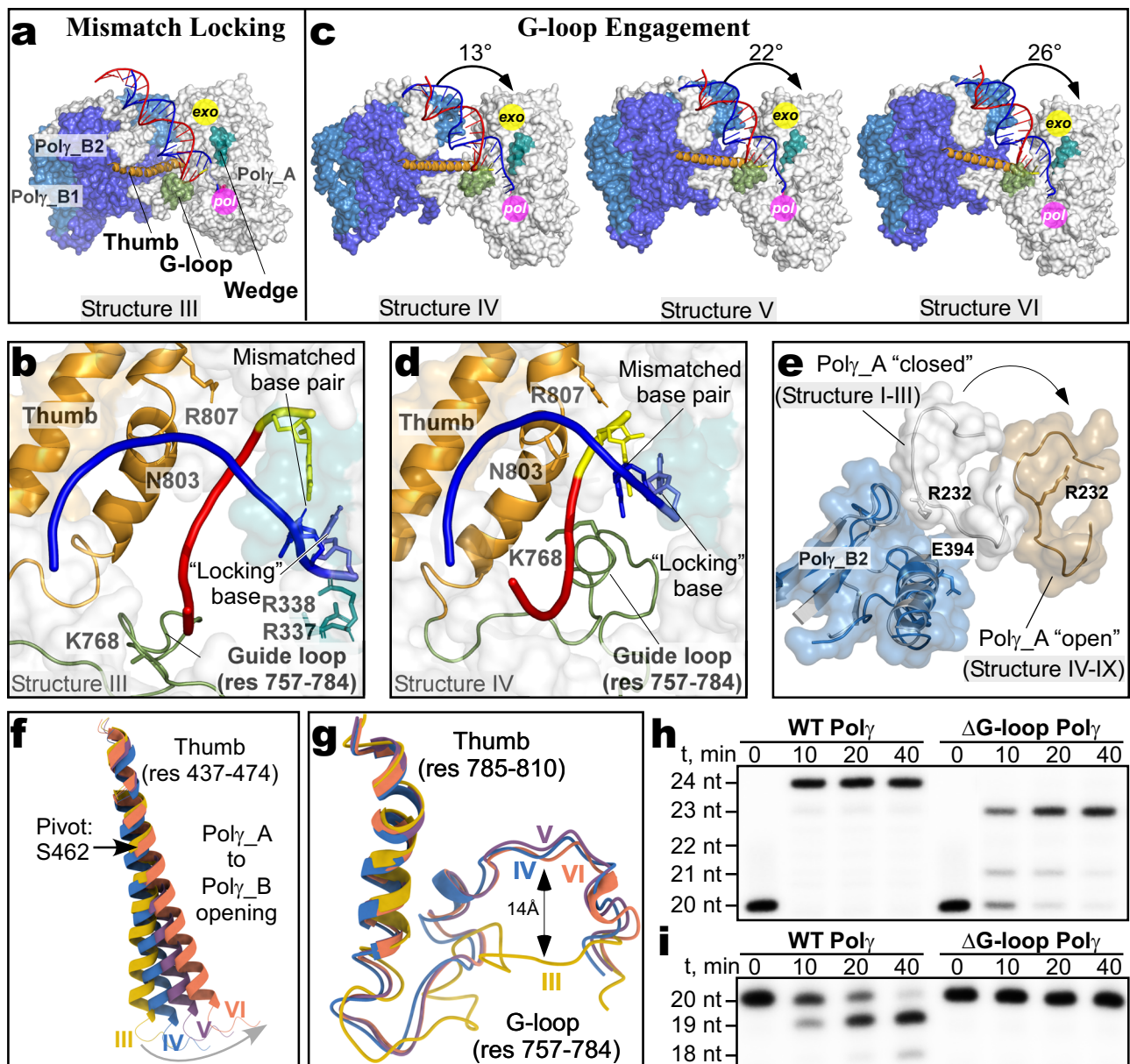


Fig. 4 | Forward translocation of Poly during proofreading. **a** Structure of the Mismatch Locking complex. The Wedge helix (teal) and the G-loop (smudge) are shown. **b** Close-up views of the 3'-end of the DNA in the Mismatch Locking complex. The $n + 1$ "locking" DNA base is shown in magenta. **c** Structures of the Guide Loop Engagement complex (Structures IV–VI). The structures are shown in the same orientation of the Poly_B homodimer as in the Mismatch Locking complex. Rotation of Poly_A (degrees) is indicated relative to the Poly_B homodimer in Structure III by the black arrow. **d** Close-up views of the 3' end of the DNA in the Guide Loop Engagement complex. The complex is shown in the same orientation of the palm

subdomain of Poly_A as in **b**. **e** Relative motion of Poly_A and the distal Poly_B2 subunits of Poly during proofreading. Conformations in Structure I (closed) and Structure VI (open) are shown. **f** Close-up view of the long helix of the thumb subdomain in Mismatch Locking (III) and G-loop Engagement (IV–VI) structures showing the bending of the thumb during forward translocation. **g** Close-up view of the G-loop in Mismatch Locking (III) and G-loop Engagement (IV–VI) structures. **h** Primer extension assay using the G-loop deletion Poly in the presence of dGTP. **i** The G-loop deletion variant of Poly is inactive in the exonuclease assay. Gels in **h**, **i** are representative results from triplicate experiments.

d). The subsequent backward translocation places the Wedge helix atop the mismatched base pair, as observed in the next captured intermediate (Wedge Alignment complex, Structure VIII, Fig. 5b, d, e). Further backtracking by 2 bp is observed in the subsequent step of proofreading, which separates the primer from the template strand and positions the 3' end in the *exo* site (The Primer Separation complex, Structure IX, Fig. 5c, f). Backtracking is defined as the process of backward translocation of polymerase along the DNA that results in a separation of the nascent RNA 3' terminus from the catalytic site and is associated with the proofreading activity of RNA polymerase²⁵. The process of backtracking is essential for many physiologically relevant

processes in bacteria and eukaryotes, such as transcription elongation, pausing, termination, fidelity, and genome instability²⁶. The observed backward translocation of Poly during proofreading suggests that backtracking may be a universal phenomenon for DNA and RNA polymerases.

In the Wedge Alignment complex, the invariant arginine residue (R309) is seen invading the space between the primer and template strand of DNA (Fig. 5e). Substitution of the R309 residue with alanine (R309A) significantly decreases Poly exonuclease activity (Fig. 5g) while not affecting its translocation (Fig. 5h). The G-loop assumes its most extended conformation, while the N803, K806, and R807

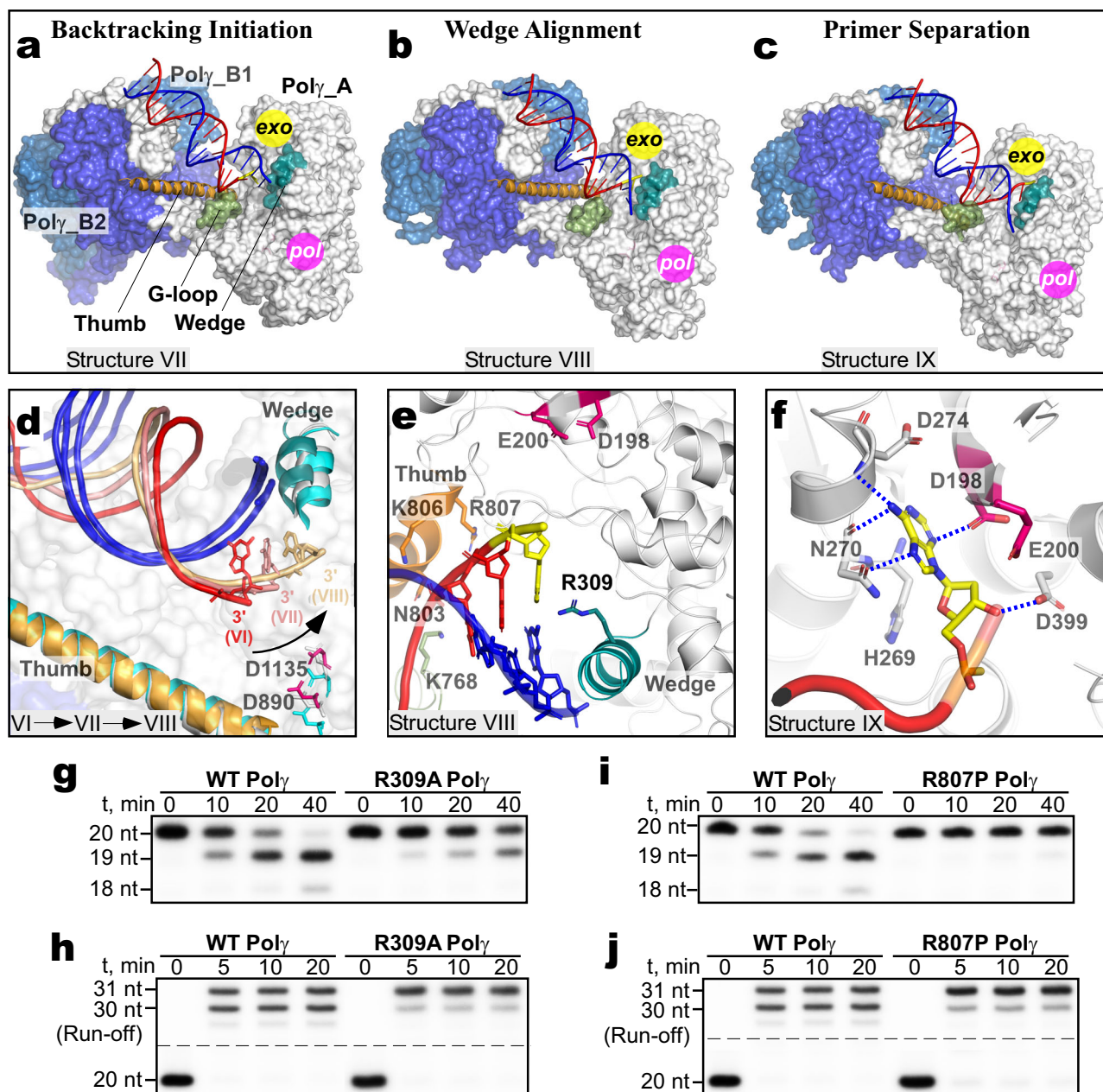


Fig. 5 | Backward translocation of Poly during proofreading. **a** Structure of the Backtracking Initiation complex. **b** Structure of the Wedge Alignment complex. **c** Structure of the Primer Separation complex. The structure is shown in the same orientation of the Poly_B homodimer as the Wedge Alignment complex in **b**. **d** Poly transition from the Guide Loop Engagement (VI) to the Backtracking Initiation (VII) and Wedge Alignment complex (VIII). The structures were aligned using their Poly_B homodimers. **e** Close-up view of the mismatched base pair at the entrance to

the exonuclease channel in the Wedge Alignment complex (**b**). The *exo* catalytic residues (D198/E200) are in pink. **f** Close-up view of the 3' end of the primer positioned in the *exo* site in the Primer Separation complex (**c**). **g**, **h** R309A Poly variant is deficient in proofreading (**g**) but active in primer extension (**h**). **i**, **j** R807P Poly variant is deficient in proofreading (**i**) but active in primer extension (**j**). Gels in **g**–**j** are representative results from triplicate experiments.

residues of the thumb subdomain additionally stabilize the DNA primer (Fig. 5e). Indeed, substituting the R807 residue with proline (R807P), a mutation found in patients with mitochondrial diseases^{27–29}, dramatically affects Poly proofreading activity (Fig. 5i) while not affecting its translocation (Fig. 5j).

In the Primer Separation complex, the backtracking of Poly pushes the Wedge helix against the mismatched base pair causing the primer to peel away from the duplex DNA and into the exonuclease channel (Fig. 5c, f). The backward motion is accompanied by a 12° rotation of the Poly_A at a pivot located at the C-terminal part of the thumb

domain (res 476) (Supplementary Video 6). In the Primer Separation structure, two terminal nucleotides in the 3' end of the primer are found in the exonuclease channel (Fig. 5c, f). The terminal base is inserted into the *exo* site and stabilized by hydrogen bonds with N270, D274, D198, and D399 residues (Fig. 5f). The proximity of the catalytic residues to the 3' end of the primer suggests that the *exo* site of Poly, similar to *E. coli* DNAP I⁴, accommodates three nucleotides of a single-stranded DNA. Therefore, Poly must backtrack one additional bp to position the phosphodiester bond between two terminal residues of the primer in the *exo* site in the Mismatch Removal complex (Fig. 2a).

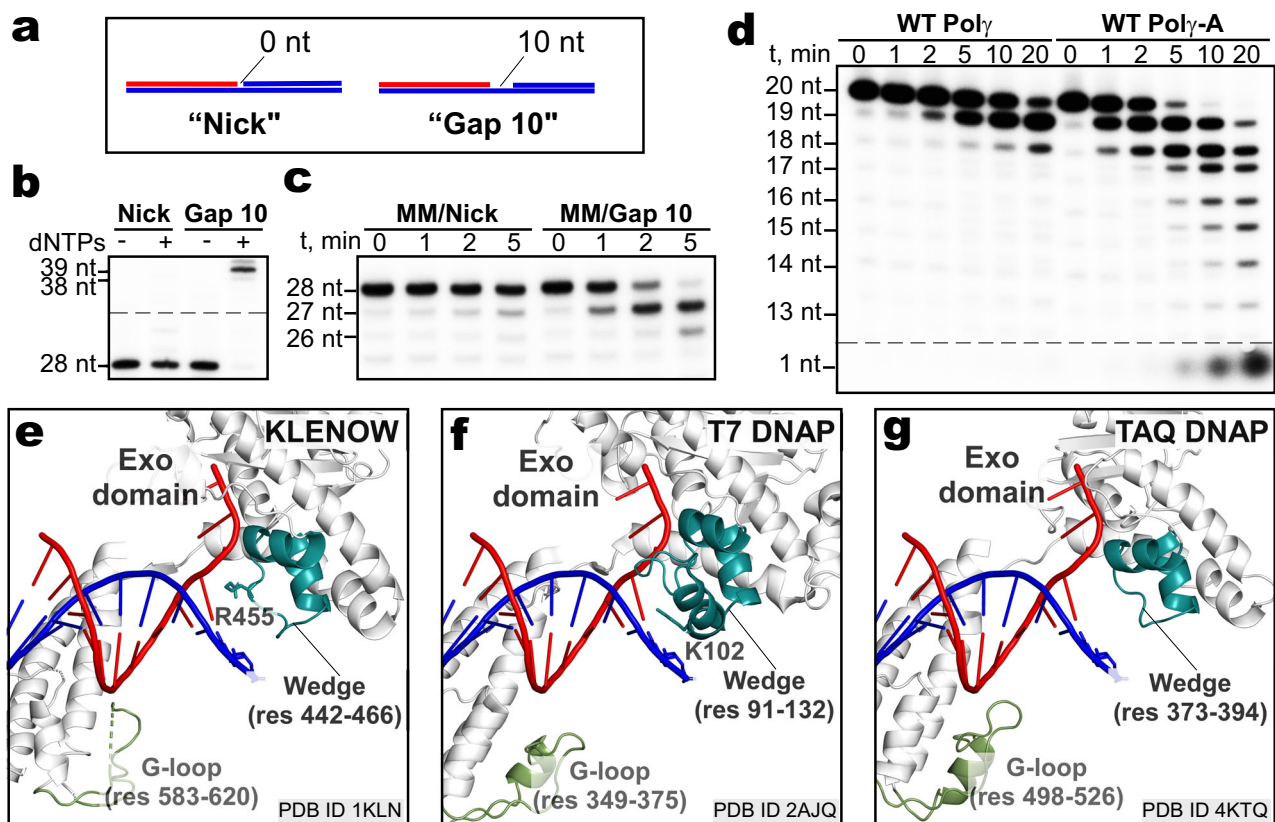


Fig. 6 | The bolt-action mechanism of proofreading. **a** Primer-templates with a nick or a 10-nt gap between the primer and downstream DNA duplex barrier used in **(b, c)**. **b** Primer extension assays performed with WT Poly in the presence of all dNTPs on scaffolds shown in **(a)**. **c** Exonuclease assay performed with WT Poly on scaffolds having a nick or 10-nt gap and a 3' end mismatched (MM) base. **d** Exonuclease assays performed with WT Poly and Poly_A. **e–g** Structural elements involved in proofreading in Poly are conserved in the Pol A family of DNAPs. Close-

up views of the major structural elements in Klenow (PDB 1KLN) **(e)**, T7 DNAP (PDB 2AJQ) **(f)**, and TAQ DNAP (PDB 4KTQ) **(g)** are shown. Structures are aligned with respect to their conserved palm subdomains. Primer-template DNA in the *exo* site **(f, g)** was modeled from the structure of the Klenow fragment (1KLN). Note that the existing T7 and TAQ structures do not reflect the proofreading step at which engagement of the G-loop is expected. Gels in **b–d** are representative results from triplicate experiments.

The “bolt-action” mechanism of proofreading

The intermediate steps of the proofreading process are represented by distinct conformations of Poly, which are stabilized by structural elements involved in the proofreading activity (Fig. 2a). These elements—the Sensor loop, the Guide loop, and the Wedge—contain highly conserved residues in mammalian species and are the hot spots for mutations that are associated with debilitating mitochondrial diseases (Supplementary Fig. 10). The prevailing point of view in the field of mitochondrial biology is that spontaneous replication errors are indeed responsible for the manifestation of mitochondrial diseases and premature aging^{1,30,31}. Importantly, the link between Poly proofreading deficiency and mitochondrial dysfunction was further established by the generation of a homozygous knock-in mouse model, termed “mtDNA-mutator” mice, and a genomically engineered fruit fly model, both expressing an exonuclease-deficient mutant of Poly_A^{32,33}. These studies have shown that Poly proofreading deficiency led to the accumulation of mtDNA point mutations and deletions, displaying reduced lifespan and premature aging-related phenotypes in the mice and embryonic lethality in the fruit flies^{32–34}. Additionally, others have identified and characterized exonuclease-deficient Poly_A mutants that are implicated in disease²⁴. Within the scope of this study, we have characterized two additional disease mutations, R309A and R807P, and have provided evidence that defects in structural elements required for Poly proofreading activity result in proofreading errors, which in turn may be responsible for mtDNA mutations and, therefore, the onset of disease and aging.

The captured states of Poly also suggest a “bolt-action” mechanism of the editing process. The “bolt-action” term refers to the iterative cycles of traversing the 3' end of the DNA primer between the two catalytic sites, first from the *pol* site to *exo* site to eliminate the mismatched base, and then from the *exo* to *pol* site to return the corrected 3' end of DNA (Fig. 2a, Supplementary Videos 1, 2). To demonstrate the importance of Poly translocation for proofreading, we prevented the enzyme's ability to advance towards the downstream DNA region by introducing a non-template strand, as a barrier, into the scaffold constructs (Fig. 6a). The presence of the non-template strand did not affect Poly binding affinity to DNA (Supplementary Fig. 11). In the absence of the replicative helicase TWINKLE, Poly was not able to unwind the DNA and translocate forward on a nick-containing scaffold but incorporated dNTPs when loaded on a gap-10 scaffold (Fig. 6b). When scaffolds with the same topology but a mismatched primer were used, proofreading was observed only on the gap-10 scaffold (Fig. 6c), confirming that forward translocation is required for proofreading.

Since mismatch removal has been prevented by the scaffold design (Complex ONE) or the use of Exo⁺ Poly (Complex TWO), we could not trap the return pathway of the corrected primer from the *exo* site to the *pol* site. Kinetic experiments suggest that this reverse pathway is much faster than delivering the mismatched base into the *exo* site¹⁶. Therefore, it is unclear if it involves the intermediate complexes described in this study. However, based on the observed changes in DNA trajectory, forward and backward translocations of Poly are expected in order to reanneal the corrected primer to the DNA template and deliver its 3' end back to the *pol* site (Supplementary Videos 1, 2).

As previously proposed, proofreading activity is associated with an equilibrium between DNAP's polymerization and proofreading modes^{15,20}. This equilibrium can be shifted by altering catalytic properties of the *pol* or *exo* sites³⁵ and mutations affecting interactions of Poly_A with Poly_B homodimer^{36–38}. Our findings suggest that during proofreading Poly_B homodimer affects the motion of the thumb subdomain of Poly, a structural element also involved in the enzyme's translocation along DNA during replication²². Indeed, in the absence of the Poly_B homodimer, the catalytic subunit of Poly exhibits strong exonucleolytic activity (Fig. 6d). However, it cannot efficiently discriminate between correct and mismatched bases, resulting in near-complete primer degradation, as evidenced by the accumulation of small cleavage products. In contrast, the holoenzyme accurately removes the mismatched base leaving the primer intact (Fig. 6d), in agreement with the proposed role of Poly_B in proofreading and replication activities^{19,39–43}.

Why doesn't Poly immediately cleave the next nucleotide upon removal of the mismatched base from the primer? Analysis of structures VIII, IX, and the modeled Mismatch Removal complex suggest that upon mismatch excision, Poly must completely withdraw the primer from the *exo* site, allowing the NMP product to diffuse out of the narrow exonuclease channel. We speculate that at this point - the conformation observed in the Wedge Alignment Structure - the pathway for the corrected primer to the *pol* site would be favored over its return to the *exo* site. We propose that the Poly_B homodimer stabilizes the Poly_A exonuclease domain, thereby controlling the NMP diffusion mechanism and progressive exonucleolytic cleavage. In contrast, the exonuclease domain in Poly_A might assume more relaxed conformation and allow faster NMP escape, promoting the processive primer degradation (Fig. 6d).

Our data suggest that the "bolt-action" mechanism of proofreading is likely conserved in Pol A family of DNAPs, which also includes proofreading *E.coli* DNA polymerase I, bacteriophage T7 DNAP, and proofreading-deficient TAQ DNAP, and human DNAPs Theta and Nu. All of these DNAPs, contain structural elements that our study demonstrates are critical for proofreading activity. Thus, in both the Klenow fragment and T7 DNAP, the Wedge helix harbors bulky amino acid residue—R455 and K102, respectively. These residues are found in a similar orientation to Poly_A R309 residue and may serve an analogous function in primer separation (Fig. 6e, f). Indeed, mutations of these residues result in dramatic changes in the proofreading activity of these enzymes^{44,45}, in agreement with the Poly_A R309 mutation phenotype demonstrated in this study. In contrast, the Wedge element in TAQ polymerase⁴⁶ does not contain any residues with the bulky side chain in the Wedge element (Fig. 6g), which likely contributes to the lack of proofreading in this enzyme⁴⁷. The G-loop element is also present in DNAP I and T7 DNAP (Fig. 6e, g); however, its role in proofreading in these polymerases has not been verified by mutagenesis or structural methods.

Our finding of distinct intermediates along the proofreading pathways in a member of the Pol A family of polymerases raises the question of whether polymerases of other families can also employ the intramolecular mechanism of proofreading^{21,48}. Since some of these polymerases have different domain organizations (such as Pol III⁴⁹) or use distinct structural elements for primer separation (e.g., the beta-hairpin in T4 DNA polymerase of the Pol B family¹⁶), the proofreading pathway likely involves different, as compared to Poly, intermediate complexes. Nevertheless, the "bolt-action" mechanism of proofreading described in this study may be a common strategy used by all processive DNA polymerases with proofreading activity.

Methods

Protein expression and purification

N-terminal histidine-tagged human Poly_B (residues 26–485) was expressed and purified as described previously⁵⁰. To express human

Poly_B, BL21-CodonPlus (DE3)-RIPL (Agilent) were transformed with the respective plasmid and grown at 37 °C in LB media until OD₆₀₀ reached 0.5 units. The proteins were induced by the addition of 0.15 mM IPTG for 18 h at 16 °C. Poly_B was purified by affinity chromatography using Ni-NTA beads (Thermo Fisher Scientific), followed by affinity chromatography using a HiTrap heparin HP column (GE Healthcare). The heparin column was equilibrated in buffer A (40 mM Tris, pH 8.0, 300 mM NaCl, 5% Glycerol, 5 mM β-mercaptoethanol), and the protein was eluted by linear gradient 0–70% of buffer B (40 mM Tris, pH 8.0, 1.5 M NaCl, 5% Glycerol, 5 mM β-mercaptoethanol). Peak fractions were pooled, concentrated, and stored at –80 °C.

Variants of N-terminal histidine-tagged human Poly_A (res 26–1239) were obtained by site-directed mutagenesis (QuikChange, Agilent). Poly_A variants (WT, G-loop deletion res 761–769, R807P, and R309A) were expressed using SF9 cells and purified as previously described for Exo' (D198A, E200A) with modifications⁵⁰. Briefly, Poly_A was purified by affinity chromatography using Ni-NTA beads (Thermo Fisher Scientific), followed by affinity chromatography using a TSKgel Heparin-5PW column (Tosoh Bioscience). The heparin column was equilibrated in buffer A (40 mM Tris-HCl pH 7.9, 150 mM NaCl, 5% Glycerol, 5 mM 2-mercaptoethanol), and Poly_A was eluted by 0–70% linear gradient of buffer B (40 mM Tris-HCl pH 7.9, 1.5 M NaCl, 5% Glycerol, 5 mM 2-mercaptoethanol). Peak fractions eluted at 33 mS/cm were collected and analyzed using SDS-PAGE, concentrated, and stored at –80 °C.

Poly holoenzyme complex was reconstituted by incubating Poly_A fractions after Ni-NTA chromatography with a twofold molar excess of purified Poly_B for 10 min at room temperature. Poly was purified by affinity chromatography on a TSKgel Heparin-5PW column (Tosoh Bioscience), equilibrated in the buffer described above. Peak fractions eluted at 40 mS/cm were collected and analyzed using SDS-PAGE, concentrated, and stored at –80 °C.

DNA and RNA oligonucleotides and scaffold preparation

Synthetic DNA oligonucleotides (IDT DNA) and synthetic RNA oligonucleotides (Dharmacon) were used. Phosphorothioate oligonucleotides were purchased as a racemic mixture of the two diastereomers. Primers sequences (all 5' to 3'): GAAGACAGTCTGCGGCGG*_A (DNA20s_A, the asterisk denotes the position of phosphorothioate, Complex ONE), GAAGACAGUCUGCGGCGGC (RNA20, Complex TWO), GAAGACAGTCTGCGGCGGC (DNA20), CCAAGTCAGAAGACA GTCTGCGGCGGC (DNA28), CCAAGTCAGAAGACAGTCTGCGGCGC GA (DNA28A), GAAGACAGTCTGCGGCGCGA (DNA20A), GGTACAAC TACGACATAGCGTG (DNA24). Template strand sequences (5' to 3'): ACACACGCGCGCCGACACTGTCTTC (DNA20TS, Complex ONE), GGTAGATCCCAGCGCCGCGACTGTCTTC (DNA20_3C_TS, Complex TWO), GGTAGATCCCAGCGCCGCGACTGTCTTC (DNA20_3C_MM_TS), CGGTGAGTACGACTCCGATTATGCGCGCCGCGACTGTCTTC TGACTTGG (DNA28TS), CGGTGAGTACGACTCCGATTATCACGCT ATGTCGTCAGTTGTACC (DNA24TS). Non-template strand sequences: TCGTGACTCGACCG (10nt gap_NT), ATAATCGGAGTCGTGACTCG ACCG (Nick_NT).

To anneal, the scaffolds were diluted in water, heated for 7 min at 95 °C, and cooled down (1 °C/min) for 1 h to 25 °C in a thermocycler.

Primer extension and exonuclease assays

The primers were 5'-[³²P]-labeled using [^γ-³²P]ATP (3000 Ci/mmol) and T4 Polynucleotide Kinase (NEB). The complexes of Poly or Poly_A (50 nM) with labeled primer-template scaffolds were assembled in a buffer containing 40 mM Tris-HCl pH 7.9, 60 mM NaCl, 10 mM MgCl₂, and 20 mM 2-mercaptoethanol in the presence of BSA (0.1 mg/ml) for 5 minutes at room temperature.

Primer extension was performed using DNA20/DNA30_3C_TS (Figs. 3h, 4g, i), "Nick" (DNA28/DNA28TS/Nick_NT, Fig. 6b), "Gap 10" (DNA28/DNA28TS/10nt gap_NT, Fig. 6b), or DNA20/DNA20TS

(Supplementary Fig. 9d) in the presence of 0.1 mM dNTPs or 1 mM dGTP, as indicated. Exonuclease assays were performed with DNA20/DNA20_MM_3C_TS (Figs. 3i, 4f, h, 6d), “MM/Nick” (DNA28A/DNA28TS/Nick_NT, Fig. 6c), or “MM/Gap 10” (DNA28A/DNA28TS/10nt_gap_NT, Fig. 6c), all of which contained a single mismatch at the 3′ terminal end of the primer. All reactions were carried out for the indicated times at room temperature and stopped by the addition of an equal volume of 95% formamide/0.05 M EDTA. The products of the reaction were resolved by 20% PAGE containing 6 M Urea and visualized by autoradiography using PhosphorImager (GE Healthcare).

Electrophoretic mobility shift assay (EMSA)

The 5′-Cy3-labeled variants of DNA24 and DNA28TS were obtained from IDT DNA (Supplementary Fig. 9a, 11a, b). To perform EMSA, complexes of Poly/DNA were assembled in a buffer containing 40 mM Tris-HCl pH 7.9, 60 mM NaCl, 10 mM MgCl₂, 5% glycerol, 20 mM 2-mercaptoethanol in the presence of BSA (0.1 mg/ml), and incubated with 150 nM of 5′-Cy3-labeled scaffolds for 10 min at room temperature. The reactions were resolved in 0.5% agarose gels run in 0.5X TBE buffer for 30 minutes at 100 V at 4 °C. The products of the reactions were visualized using Bio-Rad ChemiDoc™ imager and quantified using Bio-Rad Image Lab™. For each reaction, the fraction of bound DNA was determined as the intensity of the free DNA divided by that in the 0 nM Poly control (n = 3 independent experiments).

Preparation of Poly Complexes for CryoEM

To assemble Complex ONE, 2 μM WT Poly was mixed with the DNA20*/DNA20_TS scaffold at a 1:1.1 molar ratio in a buffer containing 10 mM Tris-HCl pH 7.9, 100 mM NaCl, 10 mM DTT, and 2 mM MgCl₂ and incubated for 5 minutes at room temperature prior to overnight dialysis at 4 °C in the same buffer.

Complex TWO (2 μM) was assembled using Exo⁺ Poly (D198A, E200A) and the RNA20/DNA20_3C_TS scaffold at a 1:1 molar ratio in a buffer described above. Following incubation at room temperature for 5 minutes, dGTP was added to a final concentration of 0.1 mM, and the primer was extended for 2 minutes at room temperature, followed by dialysis.

To assemble Complex THREE, 2 μM WT Poly was mixed with the DNA20A/DNA20_TS scaffold at a 1:1 molar ratio in a buffer containing 10 mM Tris-HCl pH 7.9, 100 mM NaCl, 10 mM DTT, and 2 mM MgCl₂ and incubated for 20 minutes at room temperature. The progression of mismatch cleavage was monitored using exonuclease assays described above.

The complexes were applied to negatively glow-discharged 300 mesh UltraAufoil -1.2/1.3 holey-gold grids (Quantifoil). Grids were blotted with ash-free Whatman® Grade 540 filter paper in a VitroBot Mark IV (ThermoFisher Scientific) for 4–5 seconds at 4 °C and 95–100% humidity, then vitrified in liquid ethane. The sample quality and distribution were assessed using Glacios Transmission Electron Microscope equipped with a Falcon 4 direct electron detector.

Single-particle data acquisition and image processing

Poly data was collected at the Pacific Northwest Center for CryoEM (PNCC) using a Titan Krios transmission electron microscope (ThermoFisher Scientific), operated at 300 kV and equipped with a Bioquantum Energy Filter with a 20 eV slit width. Movies were collected using a Gatan K3 direct electron detector in super-resolution mode with a magnification of 105,000, corresponding to a pixel size of 0.413. A dose rate of 15.9–19.3 e⁻/s/physical pixel resulted in a total electron dose of 60–70 e⁻/Å², which was applied over 60–70 frames. Data was collected in SerialEM software with defocus values ranging from -0.5 to -2.0 μm.

Workflows for image processing of Complex ONE, Complex TWO, and Complex THREE are shown in Supplementary Figs. 2–4,

respectively. The movie stacks collected for Complex ONE and Complex TWO were processed in CryoSPARC⁵¹. The super-resolution movies were frame aligned, motion corrected, gain normalized, dose-weighted, and binned twice with the patch motion correction module. Contrast transfer function (CTF) values were estimated using the patch CTF (CryoSPARC) or CTFFIND4⁵². Micrographs with ice, ethane contamination, and/or poor CTF fit resolution were discarded. A circular blob picker with dimensions of 80–130 Å was used to pick Poly particles. Local resolution plots were obtained in CryoSPARC. Resolution values for the Poly_A and Poly_B subunits were computed in RELION3.0⁵³ with focused masks (Supplementary Table 1). The reported resolutions of the CryoEM maps are based on FSC 0.143 criterion⁵⁴. The isotropy of the 3D reconstruction of Structures I–IX was estimated by 3DFSC server⁵⁵, as shown in Supplementary Figs. 5 and 6. The CryoEM density for the 3′ end of the primer in the exonuclease channel of Structure IX was improved with 3D classification in CryoSPARC 4.0.

Model building and structure refinement

Poly_A, Poly_B1, and Poly_B2 from the Poly catalytic complex (PDB ID: 4ZTZ [<https://doi.org/10.2210/pdb4ZTZ/pdb>]) were docked into the respective CryoEM maps from Complex ONE and TWO. The template, primer, and mismatched base were placed into the CryoEM density maps. The terminal mismatched guanine bases in Complex ONE structures were modeled as nonhydrolyzable phosphorothioate bases, with 50% occupancy assigned to each stereoisomer. DNA-B and RNA-A restraints from Coot were used to fit the polynucleotide chains. Additional density in Structure II resolved up to 2.6 Å resolution allowed modeling of the loop regions in Poly_B1 (res 137–161, 169–179), Poly_B2 (137–179), and Poly_A (336–340). A polyalanine model for Poly_B2 docked in a low-pass filtered map was used for Structures IV and IX. The local density fit of the modeled sequence was improved over an iterative process of amino acid fitting in Coot 0.9.8.5⁵⁶, which alternated with real-space refinement in PHENIX⁵⁷. Real-space refinement was carried out with secondary structure and Ramachandran restraints. Comprehensive model validation was carried out with PHENIX and the PDB validation server (<https://validate-rcsb-2.wwpdb.org/>) and is summarized in Supplementary Figs. 5 and 6 and Supplementary Table 2. Map-to-model Fourier Shell Correlation plots for the nine structures in Complexes ONE and TWO were obtained in PHENIX (Supplementary Figs. 5 and 6). Figures and Supplementary Videos were generated with PYMOL and ChimeraX⁵⁸.

Statistics and reproducibility

Experiments presented in Figs. 4h, i, 5g–j, and 6b–d and Supplementary Figs. 1a–c, 9b, d, and 11a, b were repeated at least three times. The representative gel images are shown.

Reporting summary

Further information on research design is available in the Nature Portfolio Reporting Summary linked to this article.

Data availability

The CryoEM maps and atomic coordinates were deposited in the Electron Microscopy Data Bank (<https://www.ebi.ac.uk/emdb>) under accession codes EMD-29745, EMD-29746, EMD-41091, EMD-29747, EMD-29748, EMD-29749, EMD-29751, EMD-29752, and EMD-29750, and in the Protein Data Bank under accession codes 8G5I, 8G5J, 8T7E, 8G5K, 8G5L, 8G5M, 8G5O, 8G5P, and 8G5N. Previously published protein structure data used for analysis in this study are available in the Protein Data Bank (www.rcsb.org) under PDB ID: 5C51 and 4ZTZ (human mitochondrial DNAP Gamma), 1KLN (Klenow fragment of *E. coli* DNAP I), 2AJQ (T7 DNAP), 4KTQ (*Thermus aquaticus* DNAP). Source data are provided with this paper.

References

- Zheng, W., Khrapko, K., Collier, H. A., Thilly, W. G. & Copeland, W. C. Origins of human mitochondrial point mutations as DNA polymerase gamma-mediated errors. *Mutat. Res.* **599**, 11–20 (2006).
- Ganai, R. A. & Johansson, E. DNA replication—a matter of fidelity. *Mol. Cell* **62**, 745–755 (2016).
- Brutlag, D. & Kornberg, A. Enzymatic synthesis of deoxyribonucleic acid. 36. A proofreading function for the 3' leads to 5' exonuclease activity in deoxyribonucleic acid polymerases. *J. Biol. Chem.* **247**, 241–248 (1972).
- Beese, L. S., Derbyshire, V. & Steitz, T. A. Structure of DNA polymerase I Klenow fragment bound to duplex DNA. *Science* **260**, 352–355 (1993).
- Hogg, M., Wallace, S. S. & Doublet, S. Crystallographic snapshots of a replicative DNA polymerase encountering an abasic site. *EMBO J.* **23**, 1483–1493 (2004).
- Reha-Krantz, L. J. DNA polymerase proofreading: Multiple roles maintain genome stability. *Biochim. Biophys. Acta* **1804**, 1049–1063 (2010).
- Bebenek, A. & Ziuzia-Graczyk, I. Fidelity of DNA replication—a matter of proofreading. *Curr. Genet.* **64**, 985–996 (2018).
- Lee, Y. S., Kennedy, W. D. & Yin, Y. W. Structural insight into processive human mitochondrial DNA synthesis and disease-related polymerase mutations. *Cell* **139**, 312–324 (2009).
- Doublet, S., Tabor, S., Long, A. M., Richardson, C. C. & Ellenberger, T. Crystal structure of a bacteriophage T7 DNA replication complex at 2.2 Å resolution. *Nature* **391**, 251–258 (1998).
- Kunkel, T. A. & Soni, A. Exonucleolytic proofreading enhances the fidelity of DNA synthesis by chick embryo DNA polymerase-gamma. *J. Biol. Chem.* **263**, 4450–4459 (1988).
- Graves, S. W., Johnson, A. A. & Johnson, K. A. Expression, purification, and initial kinetic characterization of the large subunit of the human mitochondrial DNA polymerase. *Biochemistry* **37**, 6050–6058 (1998).
- Longley, M. J., Ropp, P. A., Lim, S. E. & Copeland, W. C. Characterization of the native and recombinant catalytic subunit of human DNA polymerase gamma: identification of residues critical for exonuclease activity and dideoxynucleotide sensitivity. *Biochemistry* **37**, 10529–10539 (1998).
- Brautigam, C. A. & Steitz, T. A. Structural principles for the inhibition of the 3'–5' exonuclease activity of Escherichia coli DNA polymerase I by phosphorothioates. *J. Mol. Biol.* **277**, 363–377 (1998).
- Joyce, C. M. How DNA travels between the separate polymerase and 3'–5'–exonuclease sites of DNA polymerase I (Klenow fragment). *J. Biol. Chem.* **264**, 10858–10866 (1989).
- Carvajal-Maldonado, D., Drogalis Beckham, L., Wood, R. D. & Doublet, S. When DNA polymerases multitask: functions beyond nucleotidyl transfer. *Front. Mol. Biosci.* **8**, 815845 (2021).
- Fidalgo da Silva, E. & Reha-Krantz, L. J. DNA polymerase proofreading: active site switching catalyzed by the bacteriophage T4 DNA polymerase. *Nucleic Acids Res.* **35**, 5452–5463 (2007).
- Olson, M. W. & Kaguni, L. S. 3'→5' exonuclease in Drosophila mitochondrial DNA polymerase. Substrate specificity and functional coordination of nucleotide polymerization and mispair hydrolysis. *J. Biol. Chem.* **267**, 23136–23142 (1992).
- Lamichhane, R., Berezhna, S. Y., Gill, J. P., Van der Schans, E. & Millar, D. P. Dynamics of site switching in DNA polymerase. *J. Am. Chem. Soc.* **135**, 4735–4742 (2013).
- Johnson, A. A. & Johnson, K. A. Exonuclease proofreading by human mitochondrial DNA polymerase. *J. Biol. Chem.* **276**, 38097–38107 (2001).
- Dangerfield, T. L. & Johnson, K. A. Kinetics of DNA strand transfer between polymerase and proofreading exonuclease active sites regulates error correction during high-fidelity replication. *J. Biol. Chem.* **299**, 102744 (2022).
- Fernandez-Leiro, R. et al. Self-correcting mismatches during high-fidelity DNA replication. *Nat. Struct. Mol. Biol.* **24**, 140–143 (2017).
- Szymanski, M. R. et al. Structural basis for processivity and antiviral drug toxicity in human mitochondrial DNA replicase. *EMBO J.* **34**, 1959–1970 (2015).
- Johnson, S. J. & Beese, L. S. Structures of mismatch replication errors observed in a DNA polymerase. *Cell* **116**, 803–816 (2004).
- Ponamarev, M. V., Longley, M. J., Nguyen, D., Kunkel, T. A. & Copeland, W. C. Active site mutation in DNA polymerase gamma associated with progressive external ophthalmoplegia causes error-prone DNA synthesis. *J. Biol. Chem.* **277**, 15225–15228 (2002).
- Nudler, E., Mustaev, A., Lukhtanov, E. & Goldfarb, A. The RNA-DNA hybrid maintains the register of transcription by preventing backtracking of RNA polymerase. *Cell* **89**, 33–41 (1997).
- Nudler, E. RNA polymerase backtracking in gene regulation and genome instability. *Cell* **149**, 1438–1445 (2012).
- Di Fonzo, A. et al. POLG mutations in sporadic mitochondrial disorders with multiple mtDNA deletions. *Hum. Mutat.* **22**, 498–499 (2003).
- Sarzi, E. et al. Mitochondrial DNA depletion is a prevalent cause of multiple respiratory chain deficiency in childhood. *J. Pediatr.* **150**, 531–534 (2007).
- Del Bo, R. et al. Remarkable infidelity of polymerase gammaA associated with mutations in POLG1 exonuclease domain. *Neurology* **61**, 903–908 (2003).
- Lujan, S. A. et al. Ultrasensitive deletion detection links mitochondrial DNA replication, disease, and aging. *Genome Biol.* **21**, 248 (2020).
- Khrapko, K. et al. Mitochondrial mutational spectra in human cells and tissues. *Proc. Natl Acad. Sci. USA* **94**, 13798–13803 (1997).
- Bratic, A. et al. Complementation between polymerase- and exonuclease-deficient mitochondrial DNA polymerase mutants in genomically engineered flies. *Nat. Commun.* **6**, 8808 (2015).
- Trifunovic, A. et al. Premature ageing in mice expressing defective mitochondrial DNA polymerase. *Nature* **429**, 417–423 (2004).
- Vermulst, M. et al. DNA deletions and clonal mutations drive premature aging in mitochondrial mutator mice. *Nat. Genet.* **40**, 392–394 (2008).
- Sowers, M. L., Anderson, A. P. P., Wrabl, J. O. & Yin, Y. W. Networked communication between polymerase and exonuclease active sites in human mitochondrial DNA polymerase. *J. Am. Chem. Soc.* **141**, 10821–10829 (2019).
- Lee, Y. S., Johnson, K. A., Molineux, I. J. & Yin, Y. W. A single mutation in human mitochondrial DNA polymerase Pol gammaA affects both polymerization and proofreading activities of only the holoenzyme. *J. Biol. Chem.* **285**, 28105–28116 (2010).
- Fan, L. et al. A novel processive mechanism for DNA synthesis revealed by structure, modeling and mutagenesis of the accessory subunit of human mitochondrial DNA polymerase. *J. Mol. Biol.* **358**, 1229–1243 (2006).
- Young, M. J. et al. Biochemical analysis of human POLG2 variants associated with mitochondrial disease. *Hum. Mol. Genet.* **20**, 3052–3066 (2011).
- Farge, G., Pham, X. H., Holmlund, T., Khorostov, I. & Falkenberg, M. The accessory subunit B of DNA polymerase gamma is required for mitochondrial replisome function. *Nucleic Acids Res.* **35**, 902–911 (2007).
- Yakubovskaya, E., Chen, Z., Carrodeguas, J. A., Kisker, C. & Bogenhagen, D. F. Functional human mitochondrial DNA polymerase gamma forms a heterotrimer. *J. Biol. Chem.* **281**, 374–382 (2006).
- Longley, M. J., Nguyen, D., Kunkel, T. A. & Copeland, W. C. The fidelity of human DNA polymerase gamma with and without exonucleolytic proofreading and the p55 accessory subunit. *J. Biol. Chem.* **276**, 38555–38562 (2001).

42. Lim, S. E., Longley, M. J. & Copeland, W. C. The mitochondrial p55 accessory subunit of human DNA polymerase gamma enhances DNA binding, promotes processive DNA synthesis, and confers N-ethylmaleimide resistance. *J. Biol. Chem.* **274**, 38197–38203 (1999).
43. Johnson, A. A., Tsai, Y., Graves, S. W. & Johnson, K. A. Human mitochondrial DNA polymerase holoenzyme: reconstitution and characterization. *Biochemistry* **39**, 1702–1708 (2000).
44. Lam, W. C. et al. 3'-5' exonuclease of Klenow fragment: role of amino acid residues within the single-stranded DNA binding region in exonucleolysis and duplex DNA melting. *Biochemistry* **41**, 3943–3951 (2002).
45. Juarez-Quintero, V., Peralta-Castro, A., Benitez Cardoza, C. G., Ellenberger, T. & Briebe, L. G. Structure of an open conformation of T7 DNA polymerase reveals novel structural features regulating primer-template stabilization at the polymerization active site. *Biochem. J.* **478**, 2665–2679 (2021).
46. Li, Y., Korolev, S. & Waksman, G. Crystal structures of open and closed forms of binary and ternary complexes of the large fragment of *Thermus aquaticus* DNA polymerase I: structural basis for nucleotide incorporation. *EMBO J.* **17**, 7514–7525 (1998).
47. Kim, Y. et al. Crystal structure of *Thermus aquaticus* DNA polymerase. *Nature* **376**, 612–616 (1995).
48. Dodd, T. et al. Polymerization and editing modes of a high-fidelity DNA polymerase are linked by a well-defined path. *Nat. Commun.* **11**, 5379 (2020).
49. Scheuermann, R., Tam, S., Burgers, P. M., Lu, C. & Echols, H. Identification of the epsilon-subunit of *Escherichia coli* DNA polymerase III holoenzyme as the dnaQ gene product: a fidelity subunit for DNA replication. *Proc. Natl Acad. Sci. USA* **80**, 7085–7089 (1983).
50. Sarfallah, A., Zamudio-Ochoa, A., Anikin, M. & Temiakov, D. Mechanism of transcription initiation and primer generation at the mitochondrial replication origin OriL. *EMBO J.* **40**, e107988 (2021).
51. Punjani, A., Rubinstein, J. L., Fleet, D. J. & Brubaker, M. A. cryoSPARC: algorithms for rapid unsupervised cryo-EM structure determination. *Nat. Methods* **14**, 290–296 (2017).
52. Rohou, A. & Grigorieff, N. CTFFIND4: Fast and accurate defocus estimation from electron micrographs. *J. Struct. Biol.* **192**, 216–221 (2015).
53. Zivanov, J. et al. New tools for automated high-resolution cryo-EM structure determination in RELION-3. *Elife* **7** <https://doi.org/10.7554/eLife.42166> (2018).
54. Scheres, S. H. & Chen, S. Prevention of overfitting in cryo-EM structure determination. *Nat. Methods* **9**, 853–854 (2012).
55. Tan, Y. Z. et al. Addressing preferred specimen orientation in single-particle cryo-EM through tilting. *Nat. Methods* **14**, 793–796 (2017).
56. Casanal, A., Lohkamp, B. & Emsley, P. Current developments in coot for macromolecular model building of electron cryo-microscopy and crystallographic data. *Protein Sci.* **29**, 1069–1078 (2020).
57. Afonine, P. V. et al. Real-space refinement in PHENIX for cryo-EM and crystallography. *Acta Crystallogr. D. Struct. Biol.* **74**, 531–544 (2018).
58. Pettersen, E. F. et al. UCSF ChimeraX: structure visualization for researchers, educators, and developers. *Protein Sci.* **30**, 70–82 (2021).

Acknowledgements

We thank current and former members of the Temiakov laboratory. We are indebted to Sean Mulligan, Theo Humphreys, and Marcelo De Farias from PNCC and Tara Fox (NCI) for their expert technical assistance during data collection. We also thank Drs. William McAllister, Michael Anikin, Gino Cingolani, and Hauke Hillen for the critical reading of the manuscript and fruitful discussion. This work was supported by NIH Grant R35 GM131832 (D.T.). A portion of this research was supported by NIH grant U24GM129547 and performed at the PNCC at OHSU and accessed through EMSL (grid.436923.9), a DOE Office of Science User Facility sponsored by the Office of Biological and Environmental Research, and NIH grant S10 OD030457. This research was partly supported by the NCI's NationalCryo-EM Facility at the Frederick National Laboratory for Cancer Research under contract HSSN261200800001E.

Author contributions

Experimental design and conceptualization: G.B., A.R.N., D.T. Protein preparation and biochemical experiments: G.B., A.S., V.O.S., A.Z.O. CryoEM Data acquisition: A.R.N., K.H. Single-particle CryoEM analysis and model building: A.R.N. Writing—original draft: D.T. Writing—review & editing: D.T., G.B., A.R.N., A.Z.O.

Competing interests

The authors declare no competing interests.

Additional information

Supplementary information The online version contains supplementary material available at <https://doi.org/10.1038/s41467-023-44198-8>.

Correspondence and requests for materials should be addressed to Dmitry Temiakov.

Peer review information *Nature Communications* thanks Dong Wang and the other, anonymous, reviewer(s) for their contribution to the peer review of this work. A peer review file is available.

Reprints and permissions information is available at <http://www.nature.com/reprints>

Publisher's note Springer Nature remains neutral with regard to jurisdictional claims in published maps and institutional affiliations.

Open Access This article is licensed under a Creative Commons Attribution 4.0 International License, which permits use, sharing, adaptation, distribution and reproduction in any medium or format, as long as you give appropriate credit to the original author(s) and the source, provide a link to the Creative Commons licence, and indicate if changes were made. The images or other third party material in this article are included in the article's Creative Commons licence, unless indicated otherwise in a credit line to the material. If material is not included in the article's Creative Commons licence and your intended use is not permitted by statutory regulation or exceeds the permitted use, you will need to obtain permission directly from the copyright holder. To view a copy of this licence, visit <http://creativecommons.org/licenses/by/4.0/>.

© The Author(s) 2023